Supplementary Materials for

Seismic ocean thermometry

Wenbo Wu*, Zhongwen Zhan, Shirui Peng, Sidao Ni, Jörn Callies

*Corresponding author. Email: wenbow@caltech.edu

Published 18 September 2020, *Science* **369**, 1510 (2020)
DOI: 10.1126/science.abb9519

This PDF file includes:

Methods and materials

The principle of seismic ocean thermometry

Seismic ocean thermometry is based on the same principle as conventional acoustic tomography (*15*): measuring the travel times of sound waves to infer the average temperature of the ocean traversed by these waves. It is currently impossible to predict the absolute travel time of T waves with sufficient accuracy, however, because uncertainties in the timing and location of the source as well as in the structure of the solid earth are too great. The origin times and locations of earthquakes are typically derived using P- and S-wave travel times to a set of reference stations. Due to uncertainties in the solid-earth structure, earthquakes can be mislocated by tens of kilometers and have timing errors of a few seconds, especially if the station coverage is sparse. These uncertainties in source properties translate into uncertainties of a few seconds in the arrival time, which dominates over the sought-after signal arising from changes in the ocean temperature (Fig. 3).

We circumvent this problem by measuring relative T-wave travel times using repeating earthquakes (Fig. S1). The generation and propagation of seismic waves is sufficiently similar between repeaters that source and structure uncertainties cancel out and the change in travel time is dominated by changes in the ocean temperature. We search for repeating earthquakes based on the waveform similarity of the P wave received at a reference station (PSI in Fig. S1) and of the T wave received at the T-wave station (DGAR in Fig. S1). Because these waveforms are highly sensitive to the source locations, a high waveform cross correlation (CC) coefficient indicates overlapping earthquake locations (*32*). The relative origin time is simultaneously measured by the CC maximization at the reference station, which is then used to align the T waves and infer the travel time change $\Delta\tau'$ (Fig. S1). The structure of the solid earth does not affect this travel time change as long as changes in the solid earth between the events are negligible.

As discussed below, this is generally expected to be a very good assumption, and the travel time change $\Delta\tau'$ can indeed be attributed primarily to changes in the ocean temperature.

Sound speed dependence on temperature, salinity, and pressure

The speed of sound in seawater increases with increasing temperature, salinity, and pressure. Throughout this work, we calculate the sound speed using the Gibbs Seawater Toolbox (*42*). A typical speed of sound is $c = 1.5\ \mathrm{km\,s^{-1}}$, and a typical sensitivity of the sound speed to temperature is $\partial c/\partial T = 4\ \mathrm{m\,s^{-1}\,K^{-1}}$.

SPECFEM2D simulation and sensitivity kernel

T waves are acoustic waves trapped in a SOFAR channel, and their travel times depend predominantly on the sound speed within the SOFAR channel. This sensitivity can be quantified by travel time sensitivity kernels (*43*) (Fig. 2). Temperature-induced fluctuations in the sound speed are orders of magnitude smaller than the mean sound speed, so we are well-justified in treating these fluctuations as linear perturbations to a reference state. We base our reference state on the 2005–2015 mean temperature and salinity from the ECCO state estimate. We use a numerical simulation and its adjoint to calculate the sensitivity of the travel time to sound speed changes and subsequently convert this velocity sensitivity kernel to a temperature sensitivity kernel $K(x,z)$ using the $\partial c/\partial T$ at the reference temperature, salinity, and pressure.

A full three-dimensional simulation of *T*-wave propagation over a domain that covers thousands of kilometers is computationally expensive, so we simplify the wave propagation by restricting it to a two-dimensional depth–range problem. This is justified by the observation that at basin scales lateral refraction of sound waves in the ocean leads to only small deviations from geodesic paths (*44*). We use the Spectral Element Method (SEM) software package SPECFEM2D (*29, 45*) to simulate the wave propagation and calculate sensitivity kernels. The

SEM combines advantages of spectral and finite-element methods, which enables us to accurately simulate wave propagation in complex structures, including topography and acoustic–elastic interactions.

We take a slice along the T-wave path that is 3220 km long and 40 km deep and use realistic bathymetry along that path. The model mesh consists of 15,000 horizontal and 200 vertical elements to resolve the 2.5 Hz acoustic waves in the ocean. We use an explosive source and choose the source time function as the first derivative of a Gaussian function with a duration of 0.5 s. The source is located at a depth of 20 km and 2900 km away from the DGAR station. An explosive source gives rise to an isotropic radiation pattern of P waves, which is a good approximation to the apparent radiation pattern of an earthquake for high-frequency seismic waves (*46*).

Our structure model is composed of an ocean layer and an underlying solid earth (Fig. S2). The ocean density and sound speed are obtained by linearly interpolating the ECCO data onto SPECFEM2D model domain. We fill in edges with an average of the nearest available ECCO grid points. The solid earth has a background structure with a P-wave speed $v_p = 5800\ \mathrm{m\,s^{-1}}$, an S-wave speed $v_s = 3200\ \mathrm{m\,s^{-1}}$, and a density $\rho = 2600\ \mathrm{kg\,m^{-3}}$, which is perturbed with heterogeneities (Fig. S2). These heterogeneities in the crust, together with the rough bathymetry, produce complex scattering and multi-pathing effects and thus play crucial roles in generating long-duration T waves (*47,48*). SPECFEM2D allows us to incorporate these structure complexities into the simulation. The heterogeneities are described by a stochastic model generated using an exponential autocorrelation function with a correlation length of 2 km (*49*). Heterogeneities usually have larger v_s anomalies than v_p anomalies, so we use a root-mean-square perturbation of 3.0% for v_p and ρ and 4.5% for v_s. Note that we do not aim at fitting each wiggle of T-wave arrivals with synthetic seismograms, which is a challenging task. While a different model of the heterogeneities would produce different waveforms, it would not significantly change

the structure of the sensitivity kernel or the relative travel time change of synthetic T waves from a repeating earthquake pair, which are the key ingredients for our estimates of temperature change.

We apply a Butterworth bandpass filter (1.5 to 2.5 Hz) to the velocity seismograms of the real data before measuring their T-wave travel time changes. Accordingly, we use the same filter to process the synthetic seismogram and compute the corresponding sensitivity kernel (*50*). To obtain the sensitivity kernel, we first run a regular forward simulation to obtain the last frame of the wave field and the synthetic seismogram at the receiver. We then perform an adjoint simulation, in which the filtered and time-reversed synthetic seismogram is placed at the receiver as a virtual source, and the regular wave field is reconstructed by backward propagating the last frame of the wave field saved from the forward simulation. The sensitivity kernel is calculated by interacting the adjoint wave field with the reconstructed regular wave field (*51*).

Consistent with the expectation for sound waves trapped in the SOFAR channel, the sensitivity kernel for T waves in the 1.5 to 2.5 Hz frequency band has a peak in the SOFAR channel and decays above and below (Fig. 2B). The sensitivity kernel is nearly uniform in range, except near the two major topographic features: the Ninety East Ridge and the Afanasy Nikitin Massif. This is not surprising because these features reach the deep portion of SOFAR channel and can therefore substantially change the T-wave propagation. Such shallow topography can both block T waves and reflect them towards the receiver, which alters the structure of the sensitivity kernel (Fig. S4).

In order to investigate the reliability of our sensitivity kernel, we perform a few tests by changing the source location (depths of 10 km, 15 km, and 25 km; horizontal locations of 2950 km and 3050 km) and our model of heterogeneities in the solid earth. All tests show very nearly the same results. This indicates that the shape of the sensitivity kernel is deter-

mined almost entirely by the velocity structure in the ocean and is much less sensitive to the source properties and the structure of the solid earth. We attribute this to the multipath nature of T waves and the strong waveguide of the SOFAR channel. This insensitivity significantly simplifies the interpretation of the measured travel time changes because we do not need to recompute the kernel for each earthquake pair, which would be computationally expensive.

To test whether using a two-dimensional sensitivity kernel is justified, we calculate kernels in two additional slices: one to the north and one to the south of the central path we use throughout the rest of the study (Fig. S3). This is motivated by the observation that substantial multi-pathing can occur in the solid earth (*23, 52*). We also move the source to a 2815 km and 2950 km distance from DGAR for the northern and southern paths, respectively, which corresponds more closely to where the earthquakes are located in the northern and southern parts of the region (Fig. 1B). While there are some differences in the sensitivity kernels due to the interaction of the T waves with the distinct bathymetry along the three paths, the bulk structure of the sensitivity kernels is the same (Fig. S4). The integrated sensitivities $\iint K(x,z)\,\mathrm{d}x\,\mathrm{d}z$ are $-5.2\ \mathrm{s\,K^{-1}}$ and $-5.4\ \mathrm{s\,K^{-1}}$ along the northern and southern paths, respectively, compared to $-5.4\ \mathrm{s\,K^{-1}}$ along the central path. The slightly reduced integrated sensitivity along the northern path is largely due to the slightly shorter ocean path there (Fig. S4). This introduces an uncertainty into our conversion from travel time to temperature anomalies that is on the order of 5%. These lateral effects could be captured by three-dimensional kernel calculations in the future but are neglected here for simplicity. See "Sources of uncertainty" below for further discussion of this simplification.

Searching for repeating earthquakes and measuring *T*-wave travel time changes

Repeating earthquakes have almost identical source properties and produce seismic waveforms that are very similar to one another. This can be quantified by the waveform cross-correlation. In practice, repeating earthquakes are found by searching for earthquake pairs that have a waveform CC coefficient above a given threshold. In this study, we compute waveform CC coefficients for *P*- and *T*-waves from earthquake pairs to find repeaters, and we simultaneously measure the relative travel times between the two events. In order to reduce computational cost, we only search earthquake pairs whose cataloged locations are at most 60 km apart.

For *P* waves, we predict a travel time based on the Preliminary Reference Earth Model (*53*) and then cut the waveforms to compute the cross-correlation coefficient. In order to increase the signal-to-noise ratio, we filter the KUM and PSI records to 1 to 3 Hz and the WRAB records to 1.5 to 2.5 Hz. We choose the length of the time window over which we compute the CC coefficient as the smaller of 50 s and $6(t_S - t_P)$, where t_S and t_P are the predicted travel times of the P and S waves. The time window starts at 3 s before t_P. Then we find the peak of the CC coefficient and its associated arrival time change by fitting a quadratic curve to the discrete CC data (*54*). An example of this procedure is shown in Fig. S6. Assuming no significant temporal changes in solid-Earth properties, we attribute the *P*-wave travel time change to an origin time error in the earthquake catalog and apply this correction to the *T*-wave measurement.

T-wave travel time changes are measured similarly, albeit with different parameters. We predict the *T*-wave travel time by dividing the epicentral distance between the source location and DGAR by a constant velocity of 1.51 $\mathrm{km\,s^{-1}}$. Predicting an accurate *T*-wave travel time is more difficult than for solid earth phases (e.g. for direct *P* waves) because *T*-wave propagation paths are more complex and travel times are more sensitive to errors in the source location. By manually examining the *T*-wave data we found that 1.51 $\mathrm{km\,s^{-1}}$ is an appropriate number for

most observations. We note that a large discrepancy between the predicted and true travel times may be present for some data, which would cause our T-wave detection to fail and thus reduce the number of measurements. This situation is not common, however, and does not generate any systematic bias in our final result. We measure the T-wave travel time change using a 60 s long time window that starts 10 s after the predicted T-wave arrival time.

We use a CC coefficient threshold of 0.9 for P waves to detect repeating earthquakes and a lower threshold of 0.6 for T waves to obtain a large number of measurements. We note that there remain uncertainties in detecting repeating earthquakes based on waveform cross-correlation (*32*), and discrepant source locations could affect our measurements of T-wave travel time changes. We use a relatively long time window for waveform CC, however, which lowers the chance of large source discrepancy. The effects of location discrepancies turn out to be much smaller than the travel time anomalies caused by ocean temperature changes (see "Sources of uncertainty" below).

Signal-to-noise ratio of T-wave arrivals

The excellent performance of the DGAR station in recording T waves is demonstrated by the histogram of signal-to-noise ratios for T-wave arrivals in Fig. S5. We define the signal-to-noise ratio as the ratio between the T-wave amplitude and the noise amplitude. The T-wave amplitude is measured over a time window between 50 s before and 100 s after the predicted T-wave arrival time. The noise window is taken from 200 s to 50 s before the T-wave arrival time. More than half of the earthquakes with $M > 4.25$ have T-wave arrivals with a signal-to-noise ratio greater than or equal to 2.0. The T-wave data become noisy for $M < 4.0$.

According to the Gutenberg–Richter law (*40*), the number of earthquakes should increase exponentially with decreasing magnitude. The ISC earthquake catalog we are using, however, obviously does not follow this law at magnitudes less than 4.0. This discrepancy indicates that

the catalog is incomplete for small earthquakes ($M < 4.0$), which is not surprising given that the global seismic network has a limited detection capability for such small earthquakes.

T waves from the repeating earthquake pair on 21 October 2006 and 3 March 2008

We linearly interpolate the daily ECCO temperature data to 21 October 2006 11:53 and 3 March 2008 20:05 (Fig. S7), which are the origin times of the repeating earthquakes used in Fig. 2. We then derive the sound speed and density structures and run SPECFEM2D to obtain synthetic seismograms (Fig. S8). The synthetic waveforms of the *T* waves produced by these events are very similar, which indicates that only minor waveform changes should be expected to be caused by the ocean temperature variations. The travel time change of the synthetic *T* waves is measured with the same cross-correlation method as applied to the observed data. The travel time decrease is $\Delta\tau' = -0.145$ s (Fig. S8), which exactly matches the $\Delta\tau' = -0.145$ s obtained using the sensitivity kernel (Fig. 2).

Timing correction

A *T*-wave time delay of more than 1 s appears in the data after March 2012 (Fig. S9). This time shift is so large that the most likely explanation is an error in the seismometer's timing system. We note that this anomaly is present in all measurements, irrespective of which reference station is used, so it must be due to a timing issue at DGAR rather than a reference station. Timing errors are not rare for seismometers, especially before the 2000s when GPS clocking systems became widespread. Inspection of the DGAR instrumentation history shows a sensor system upgrade on 17 March 2012, which is the most likely date of the erroneous time shift.

To remove this timing inconsistency, we use two pairs of repeating earthquakes with moderate magnitudes that were well-documented by Yao et al. (*55*). The relative origin times of these doublet earthquakes have been accurately constrained using a number of mantle *P* waves, and

we received this information from Yao et al. through personal communication. The repeating earthquakes on 11 October 2005 and 10 January 2013 have large magnitudes of 6.0 and 5.9, respectively, and therefore generate clear short-period *P*-wave arrivals at DGAR (Fig. S10). We cross-correlate these waveforms and find a time delay of 1.01 s. We note that the CC coefficient of 0.74 is relatively low because noise is present in the record and the rupture processes of the earthquakes were possibly different. Another pair of repeating earthquakes on 5 January 2005 and 5 June 2012 has smaller magnitudes of 5.4 and 5.6 and produces weak short period body waves hidden in the noise. We therefore instead use the long-period *S* and Rayleigh waves and obtain a time shift of 1.03 s (Fig. S10). The consistency between these two time delays supports our interpretation of the time shift as a timing error, and we take the average number of 1.02 s to calibrate the data from earthquake pairs that cross 17 March 2012. After this calibration, most *T*-wave travel time changes are within a range of ± 0.4 s (Fig. S11), consistent with the data involving events from before 17 March 2012 only.

Inversion and uncertainty estimation

We use a simple inversion to turn the measured travel time changes $\Delta\tau'_k$ for event pairs $k = 1,\ldots,n$ into a time series of travel time anomalies τ'_i at the unique event times t_i with $i = 1,\ldots,m$, relative to an arbitrary but common reference. Part of this inversion is over-constrained because some events are paired with more than one other event, and the measured travel time changes are not generally mutually consistent. Our inversion therefore minimizes the mismatch between the measured and inverted travel time changes. Part of the inversion, however, is under-constrained because not all events are connected by pairs. We therefore regularize the inversion by simultaneously minimizing the curvature of the time series. We choose to be agnostic about the timescale on which the underlying time series is smooth and apply the curvature minimization on the timescale set by the sampling interval. This allows us to resolve high-frequency

variations early in the record, where the sampling is fine, while simultaneously constraining the long-term record. We hence minimize the cost function

$$J = \frac{1}{2}\sum_{k=1}^{n}\left(\tau'_{i(k)} - \tau'_{j(k)} - \Delta\tau'_k\right)^2 + \frac{1}{2}\sum_{i=2}^{m-1}\left[\frac{t_{i+1}-t_{i-1}}{2}\left(\frac{\tau'_{i+1}-\tau'_i}{t_{i+1}-t_i} - \frac{\tau'_i - \tau'_{i-1}}{t_i - t_{i-1}}\right)\right]^2, \quad (3)$$

where $i(k)$ and $j(k)$ denote the indices of the event pair k. We additionally constrain the τ'_i to sum to zero, which sets the arbitrary reference travel time.

To estimate the uncertainty of the travel time change measurements, we calculate the RMSE

$$\sigma_\Delta = \sqrt{\frac{1}{n-m-1}\sum_{k=1}^{n}\left(\tau'_{i(k)} - \tau'_{j(k)} - \Delta\tau'_k\right)^2}. \quad (4)$$

We propagate this uncertainty estimate for $\Delta\tau'_k$ to the estimated τ'_i by calculating the pseudoinverse of the Hessian associated with the above optimization problem. The standard errors for τ'_i are the square roots of the diagonal elements of this pseudoinverse multiplied by σ_Δ. Note that the error estimate is not independent of the curvature constraint we added to the cost function.

Cycle-skipping correction

We measure the T-wave travel time change by searching for the peak of the CC coefficient, which suffers from the common problem of cycle skipping. Cycle skipping happens when the measured time shift is more than one period away from the true time shift. The dominant period of the T-wave signals we use is 0.5 s, so cycle skipping generally shifts the measurement by more than 0.4 s. The repeating earthquake pair in Fig. S12 shows a typical example of cycle skipping. The T-wave travel time change is obtained at a peak CC coefficient of 0.68, while the secondary peak to the right has a CC coefficient of 0.66. It would be difficult to determine which one is the correct number in the presence of noise and waveform changes due to source property discrepancies.

To solve this problem, we measure both the peak CC coefficient and the two adjacent side lobes. We use the inversion described above to decide whether or not to apply a cycle-skipping

correction. We apply a cycle-skipping correction if it reduces the cost function and if the difference in the CC coefficient is less than 0.15. We apply a local search for these cycle-skipping corrections, which converges quickly with a total of 16 cycle-skipping corrections. These 16 corrected pairs constitute less than 0.5% of the total number of measurements (Fig. S13). The RMSE after this correction is $\sigma_\Delta = 0.032$ s. The distribution of residuals is more peaked than a Gaussian with this standard deviation because the number of parameters $m = 901$ is a substantial fraction of the number of constraints $n = 3380$ (Fig. S13).

This cycle-skipping correction can only correct cases in which one cycle was skipped. It is possible that multiple cycles are skipped, although the chance of this occurring is very low. If present in our data, pairs affected by a skipping of multiple cycles have a travel time change larger than 0.8 s and are flagged as outliers (anomalies larger than 0.65 s).

Sources of uncertainty

A few factors other than ocean temperature anomalies could produce *T*-wave travel time anomalies. These factors include source location discrepancies between the repeating earthquakes, temporal change in the solid earth, tidal currents, non-tidal currents, salinity anomalies, noise in the seismic records, and errors in the SPECFEM2D modeling. The latter two sources of uncertainty were discussed in previous sections.

Source location discrepancies are likely the largest source of uncertainty in this study. These discrepancies affect not only the *T*-wave travel times but also the *P*- and *S*-wave travel times estimated at the reference stations. Comparing the relative origin times derived from the different reference stations can thus help assess this effect. The corrections from the three stations are consistent for most repeating earthquake pairs (Fig. S14). Most results from WRAB–PSI, WRAB–KUM, and PSI–KUM have discrepancies smaller than 0.02 s. Only two data points show large deviations. These two outliers are due to problematic KUM measurements and have

a consistent discrepancy of 4.9 s, very likely due to a timing issue at KUM. We exclude these two outliers from our analysis. The discrepancies between the different reference stations have a similar spread as the final residuals of our inversion (Fig. S13). This suggests source location discrepancies and/or random noise contamination might be the main source of uncertainty, which justifies treating measurements involving the same events but different reference stations as independent in the inversion.

The temporal change of the solid earth should be smaller 0.05 s. This is supported by previous studies (*33*) and by our comparison of the origin times derived from the three different reference stations KUM, PSI, and WRAB (Fig. S14).

Depth-independent tidal currents that Doppler shift T waves in the East Indian Ocean have amplitudes around 0.02 $\mathrm{m\,s^{-1}}$ (*56*). These currents occur on basin scales and can therefore cause travel time anomalies between Sumatra and Diego Garcia of about 0.03 s. We make no attempt to correct for this effect, so only travel time variations substantially larger than this amplitude should be interpreted as being caused by temperature anomalies. The earthquakes occur at random phases of the tidal cycle, so this effect should not alias into longer-period variability.

We estimate the effect of non-tidal currents and salinity anomalies using the ECCO state estimate. As for the temperature anomalies, we interpolate the daily ECCO data onto the times of the events and estimate the corresponding travel time anomalies using the sensitivity kernel. Both effects are much smaller than the temperature effect and can be neglected (Fig. S15).

In addition to the aforementioned factors, uncertainties in the interpretation of the travel time data is introduced by assuming that all earthquake pairs sample the same part of the ocean. If we interpolate ECCO data onto the three paths shown in Fig. S3 and infer travel times with the respective kernels (Fig. S4), we find only modest differences between the three paths (Fig. S16). The anomalies introduced by lateral variations are generally small compared to the temporal

anomalies, supporting our interpretation of the travel time data.

The lateral variations in the sensitivity kernel and in the temperature anomalies also introduce some uncertainty in the magnitude of the temperature trends estimated from ECCO and the T waves. Table S1 lists the trends computed along the three paths. For ECCO, we use the temperature anomalies interpolated onto the respective path and the weighting implied by the respective kernel (Fig. S4). For the T-wave data, we use the respective bulk sensitivities. While the trends differ by a few millikelvin per decade between the paths, the trend estimated from the T-wave data is larger than that estimated from ECCO along all paths. The lateral variations are therefore unlikely to be the source of the discrepancy between the two datasets.

	ECCO trend	T-wave trend
northern path	0.040 ± 0.001	0.046 ± 0.002
central path	0.039 ± 0.001	0.044 ± 0.002
southern path	0.038 ± 0.001	0.044 ± 0.002

Table S1: Trends (in Kelvin per decade) calculated along the three paths in Fig. S3. For the ECCO trends, the temperature data is interpolated onto the respective path and weighted using the respective sensitivity kernel. For the T-wave trends, the trend in travel time anomalies is converted to a temperature trend using the slightly different bulk sensitivities along the three paths.

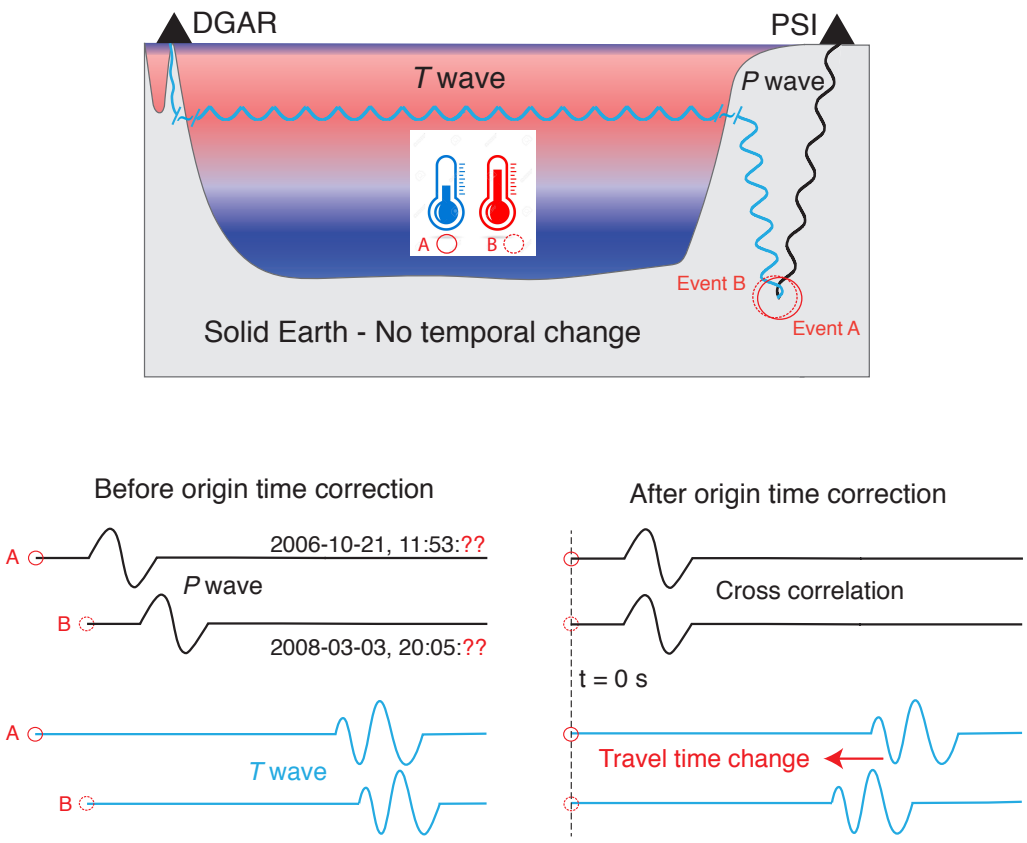

Figure S1: Principle of seismic ocean thermometry. (Top) Schematic of ocean seismic thermometry with repeating earthquakes. The two red circles show the overlapping locations of repeating earthquakes A and B. DGAR is the T-wave station and PSI is the reference station recording P waves. (Bottom) Schematic illustrating the procedure of measuring the T-wave travel time change. The left panel shows the P- and T-wave seismograms from the repeating earthquakes A and B. The right panel shows the waveforms after alignment on the earthquake origin times, derived from the cross correlation of the P waves at the reference station.

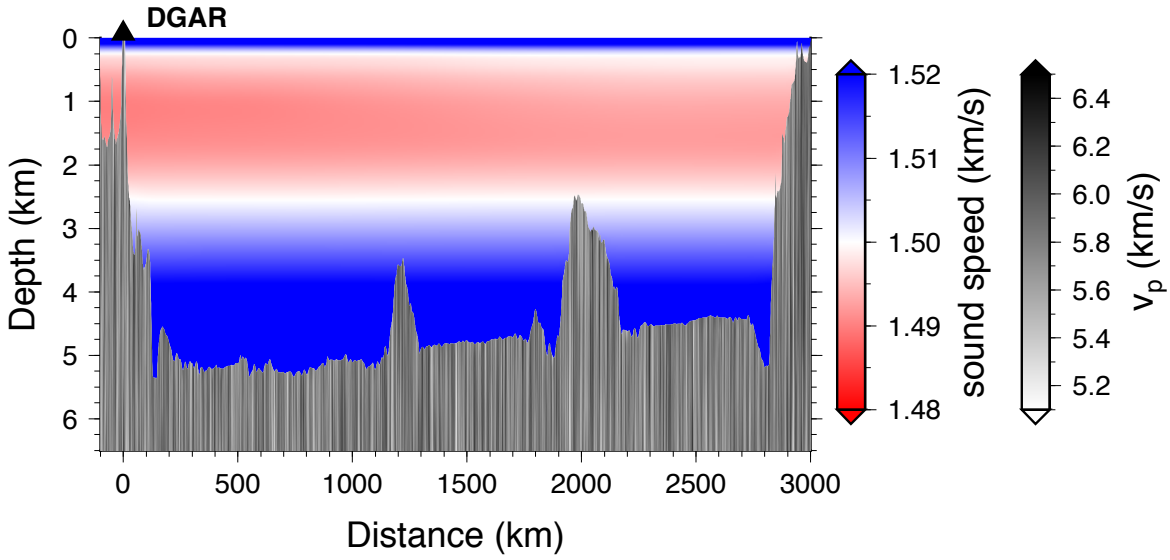

Figure S2: Velocity model for the SPECFEM2D simulation. Shown are the acoustic speed in the ocean and the v_p model with random velocity perturbations in the solid earth. Note the different scales in the horizontal and vertical directions. The black triangle shows the location of the DGAR station.

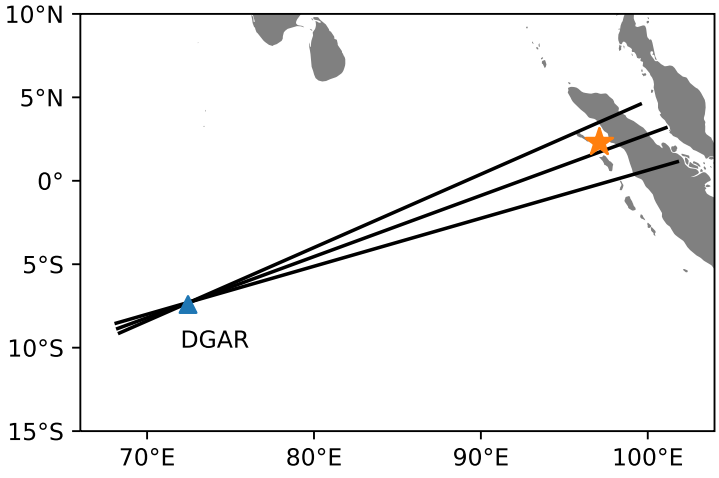

Figure S3: Locations of the three two-dimensional model domains used in this study. The central path is used throughout the main text, and the other two paths are used to test the results' sensitivity to variations in the cross-path direction. The orange star shows the hypocenter of 2005 M 8.6 earthquake.

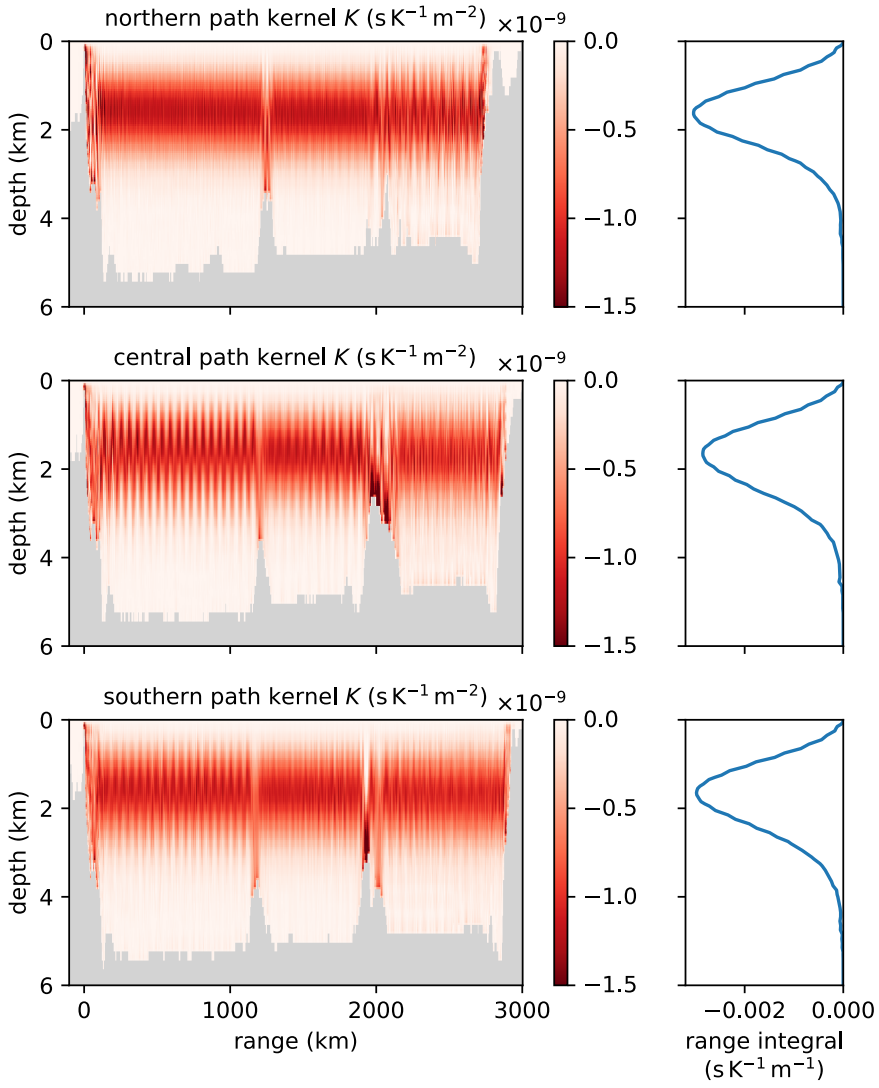

Figure S4: Sensitivity kernels for the three paths shown in Fig. S3. Shown are the full two-dimensional kernels (left) and the range integrals (right). The bathymetry is shown in gray.

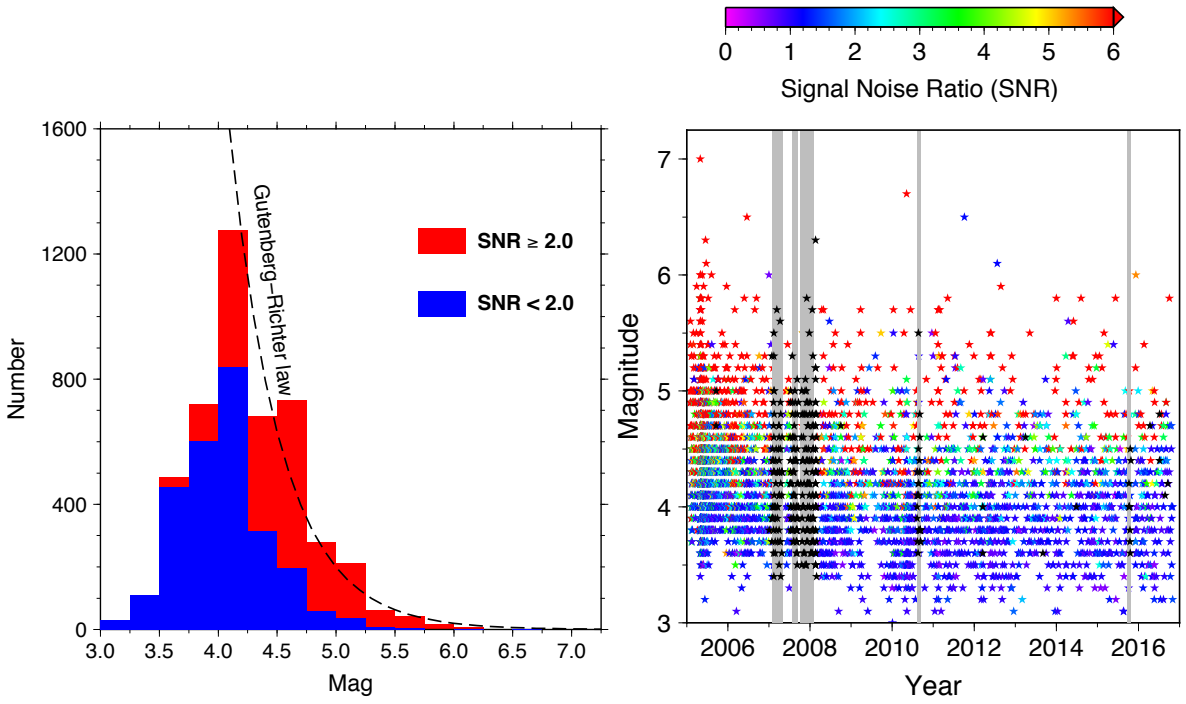

Figure S5: Signal-to-noise ratios (SNR) for the *T*-wave arrivals. (Left) SNR histogram by earthquake magnitudes. The dashed line shows the Gutenberg–Richter law, which predicts an exponentially increasing number of earthquakes with decreasing magnitude. (Right) SNR as a function of time and magnitude. The gray bars show DGAR data gaps with a duration longer than 30 days. Earthquakes within the data gaps are colored in black.

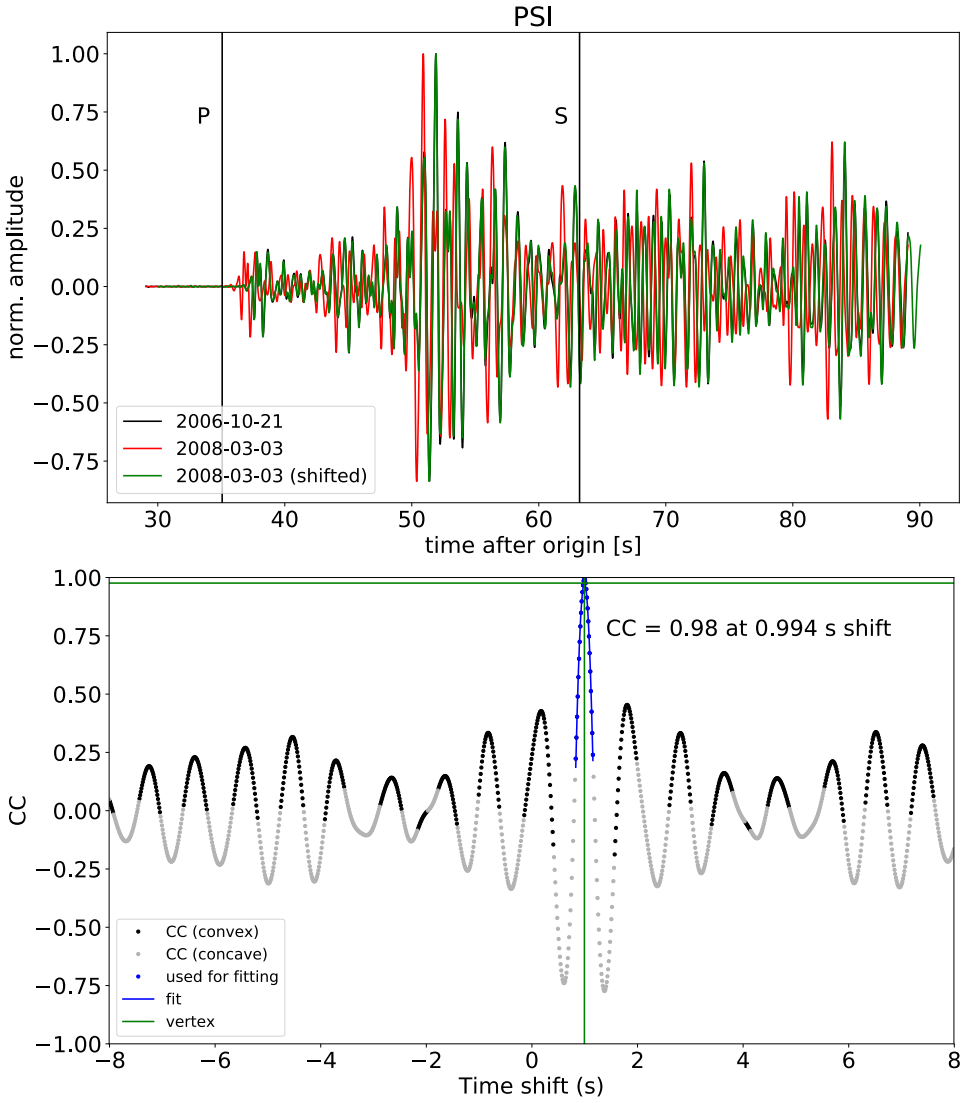

Figure S6: An example of the earthquake origin time correction using the cross-correlation of *P* and *S* waves from the PSI station. (Top) Normalized *P*- and *S*-wave arrivals from a repeating earthquake pair. The two black vertical lines mark the predicted arrival times of these waves. The green line shows the waveform of the 3 March 2008 earthquake shifted by 0.994 s, which is derived by maximizing the cross-correlation between the two waveforms. (Bottom) Cross-correlation function between the two waveforms. The origin correction is taken as the peak of the CC, marked by the horizontal and vertical green lines and derived by fitting a quadratic curve (blue line) to the discrete points of the convex part of the CC around the peak CC (blue dots).

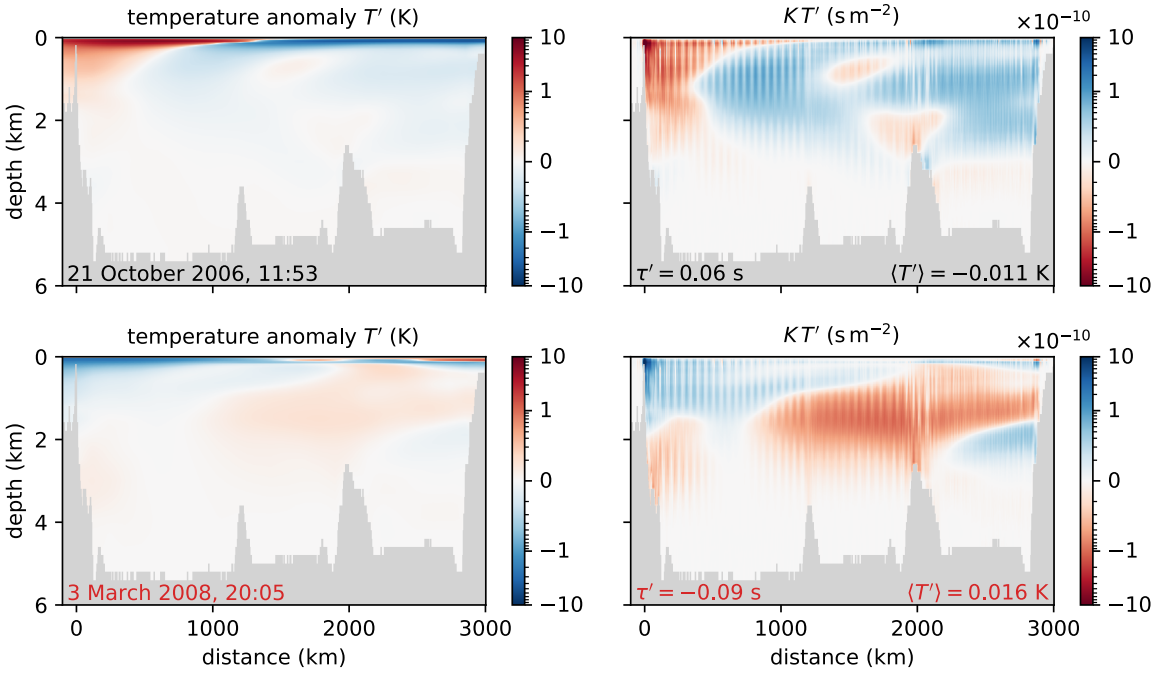

Figure S7: ECCO temperature anomalies for the repeating earthquake pair in Fig. 2. The temperature anomalies are referenced to the long-term mean (2005–2015) (left) and the corresponding contributions to the travel time anomalies are calculated using the sensitivity kernel K (right).

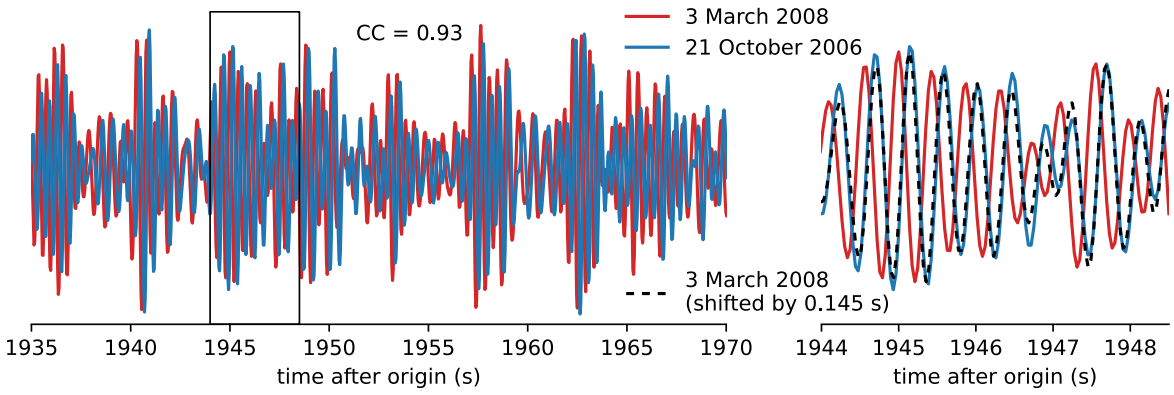

Figure S8: Synthetic T-wave seismograms for the repeating earthquake pair in Fig. 2. The waveforms for the 21 October 2006 and 3 March 2008 events are shown in blue and red, respectively. The dashed black line shows the 3 March 2008 waveform shifted by 0.145 s, as determined by maximizing the cross-correlation. The right figure displays a zoom-in on the part of the waveforms marked by the dashed rectangle.

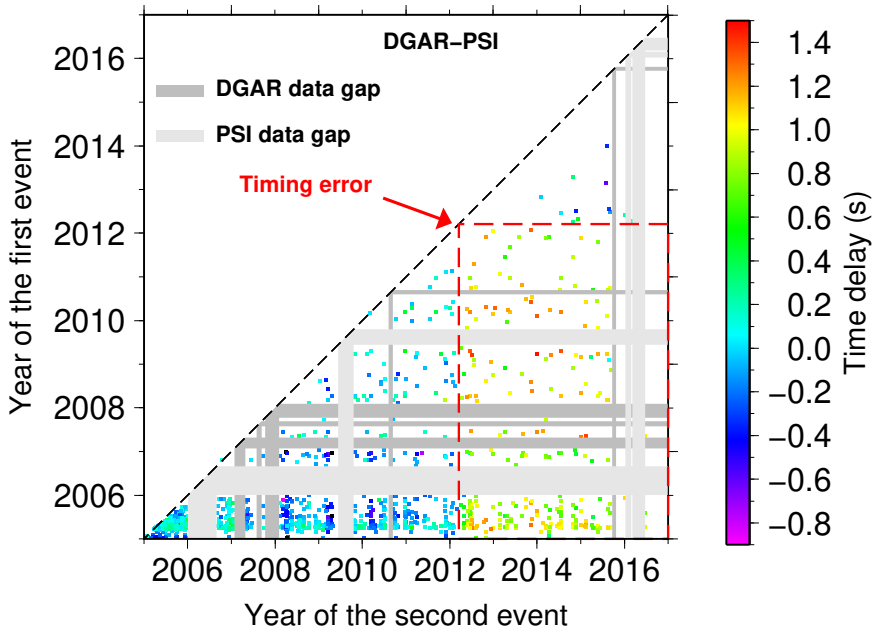

Figure S9: T-wave travel time changes inferred using PSI as a reference station. The color represents travel time change. An obvious timing error occurred in March 2012. The horizontal and vertical axes show the times of paired repeating earthquakes. The dark gray and light gray bands show data gaps longer than 30 days.

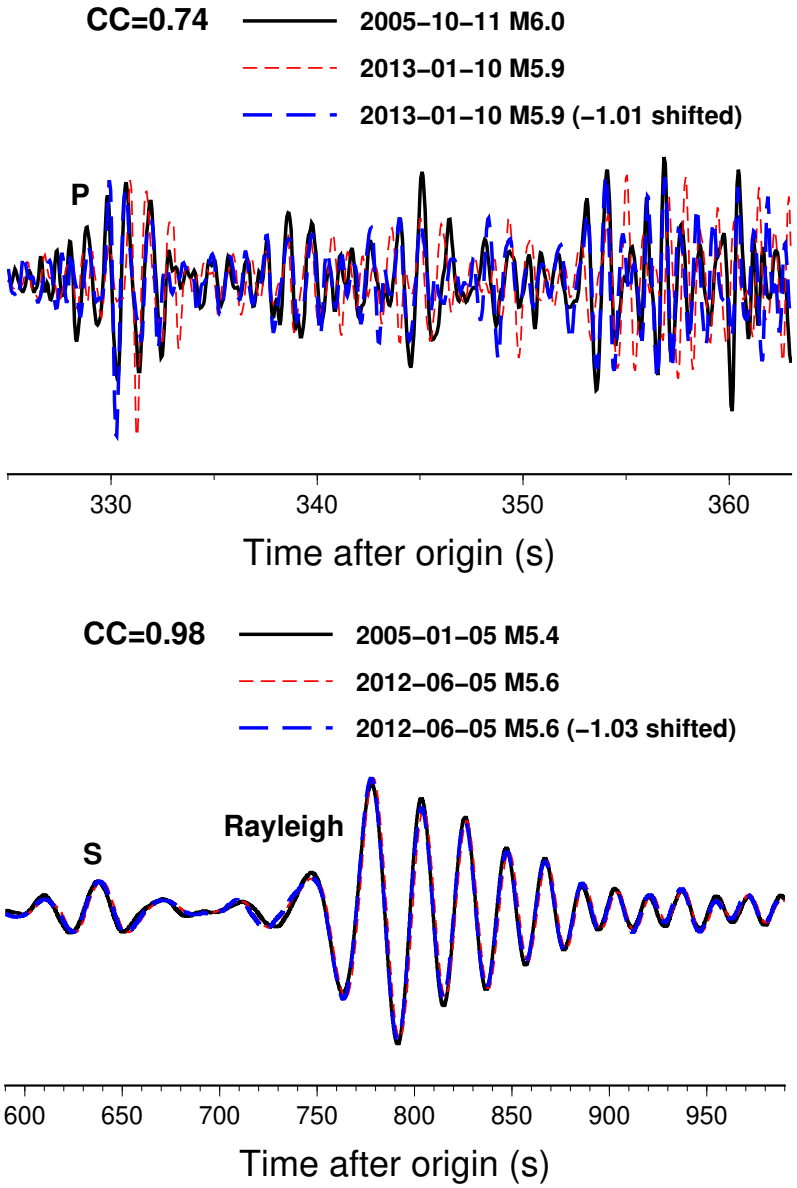

Figure S10: Timing correction using two doublets. (Top) Waveforms from the doublet on 11 October 2005 and 10 January 2013. The black line shows the 1.0 to 3.0 Hz vertical component of the velocity seismogram of the 11 October 2005 event, and the red dashed line shows the same data for the 10 January 2013 event. The cross-correlation is maximized at a time shift of 1.01 s, which we attribute to a timing issue at DGAR. The major signals from the earthquakes in this time window are the direct *P* and its coda waves. (Bottom) Waveforms (0.02 to 0.05 Hz) from the doublet on 5 January 2005 and 5 June 2012. The cross-correlation is maximized at a time shift of 1.03 s. The major phases in this time window are *S* and Rayleigh waves.

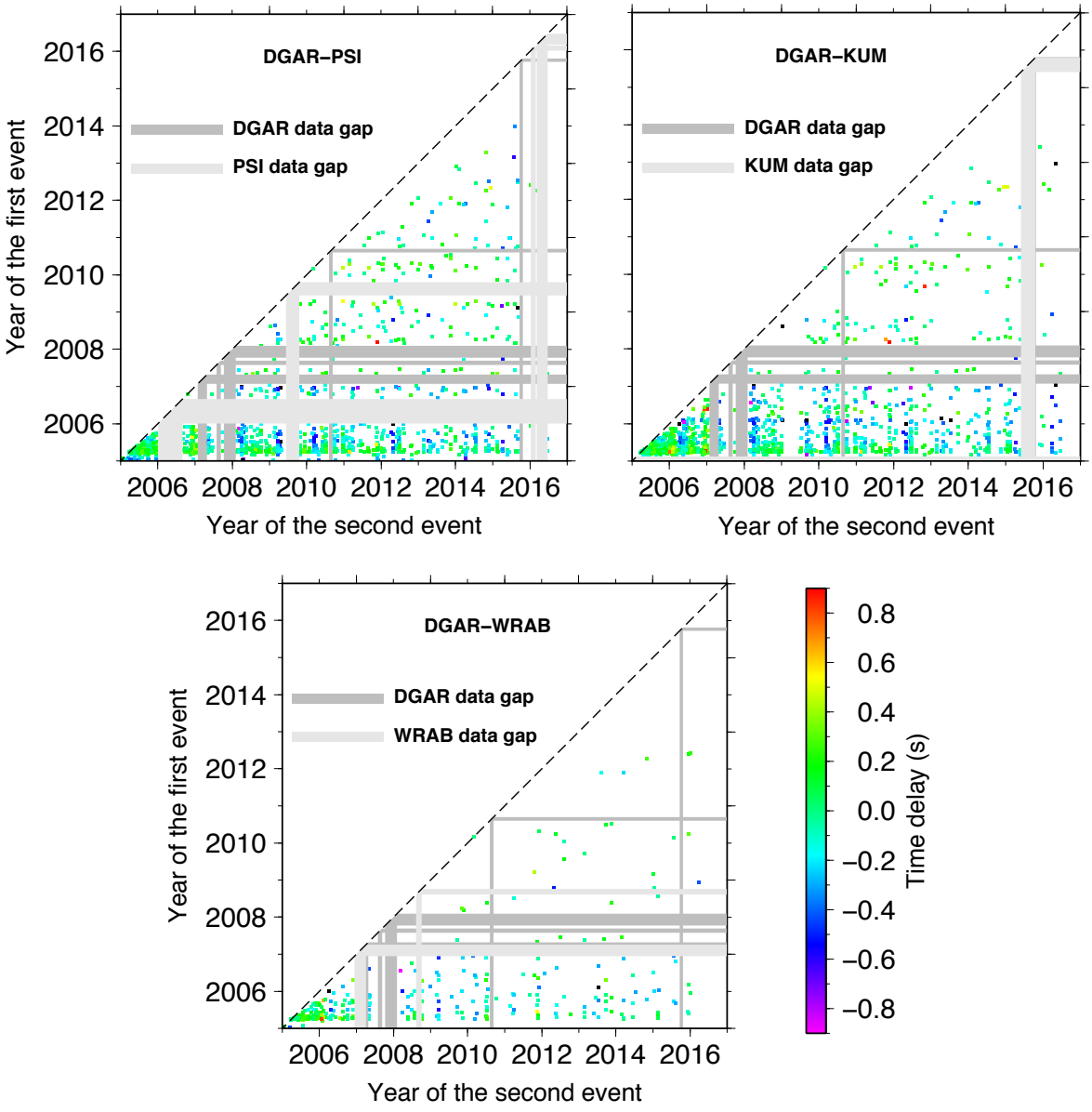

Figure S11: *T*-wave travel time changes after the timing correction. Separate panels are shown for the three reference stations PSI, KUM, and WRAB. WRAB provides fewer event pairs with high CC than PSI and KUM because it is farther from the origin and thus generally has a lower signal-to-noise ratio for *P* waves. Note that the color bar has a different scale from that in Fig. S9. The horizontal and vertical axes show the times of paired repeating earthquakes. The dark gray and light gray bands show data gaps longer than 30 days.

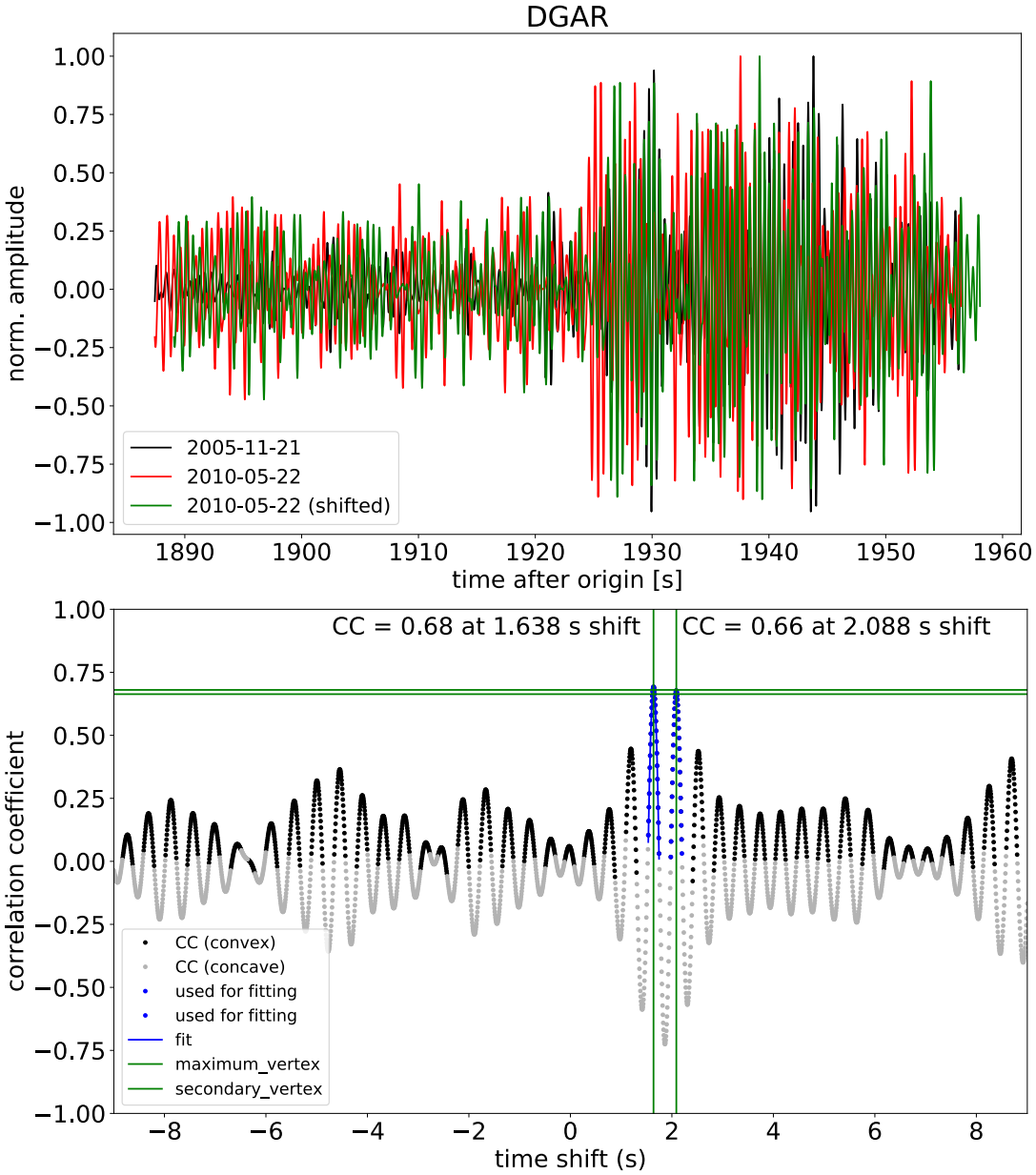

Figure S12: An example of cycle skipping in the measurement of the T-wave travel time change. (Top) Normalized T-wave arrivals from a repeating earthquake pair. The green line shows the waveform of the 22 May 2010 earthquake shifted by 1.638 s, which is derived by maximizing the cross-correlation between the two waveforms. (Bottom) Cross-correlation function between the two waveforms.

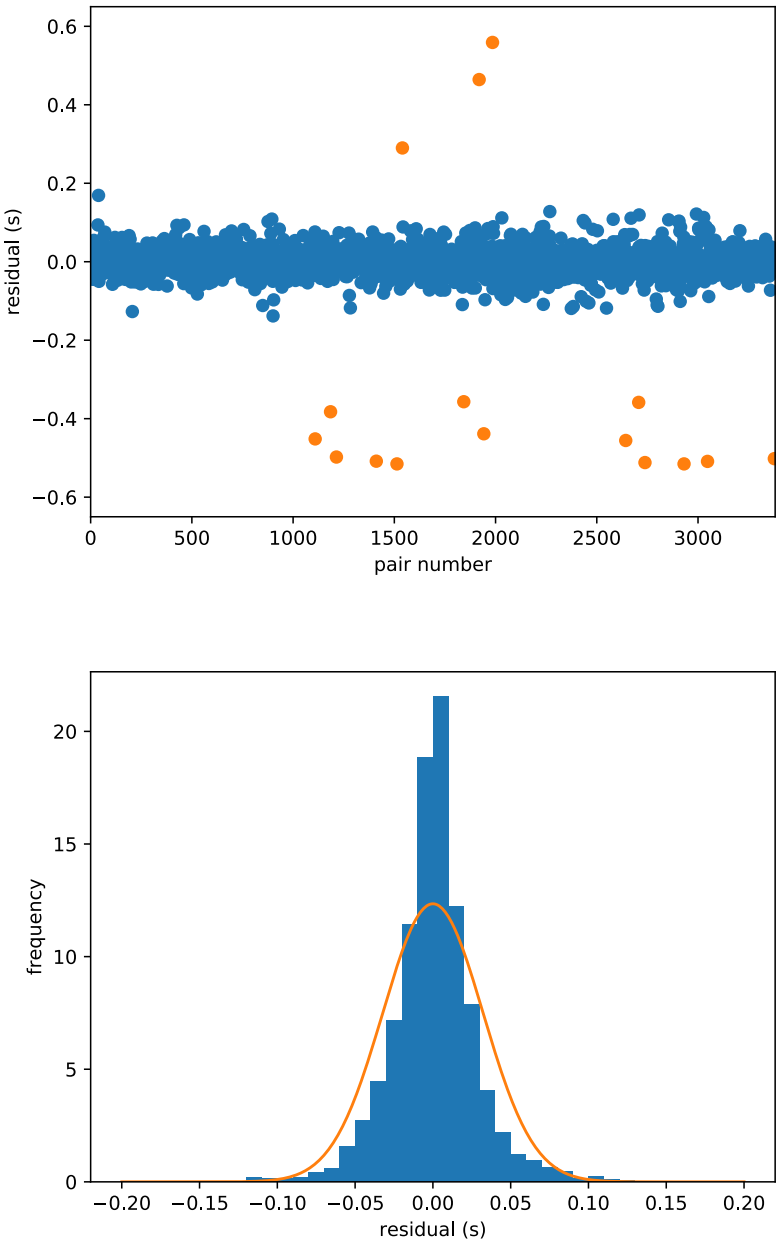

Figure S13: Residuals before and after the cycle-skipping correction. (Top) Residuals before the cycle-skipping correction plotted against the pair number k. The 16 event pairs that a cycle-skipping correction is applied to are shown in orange. (Bottom) Normalized histogram of the residuals after the cycle-skipping correction. The normal distribution based on the RMSE is shown in orange.

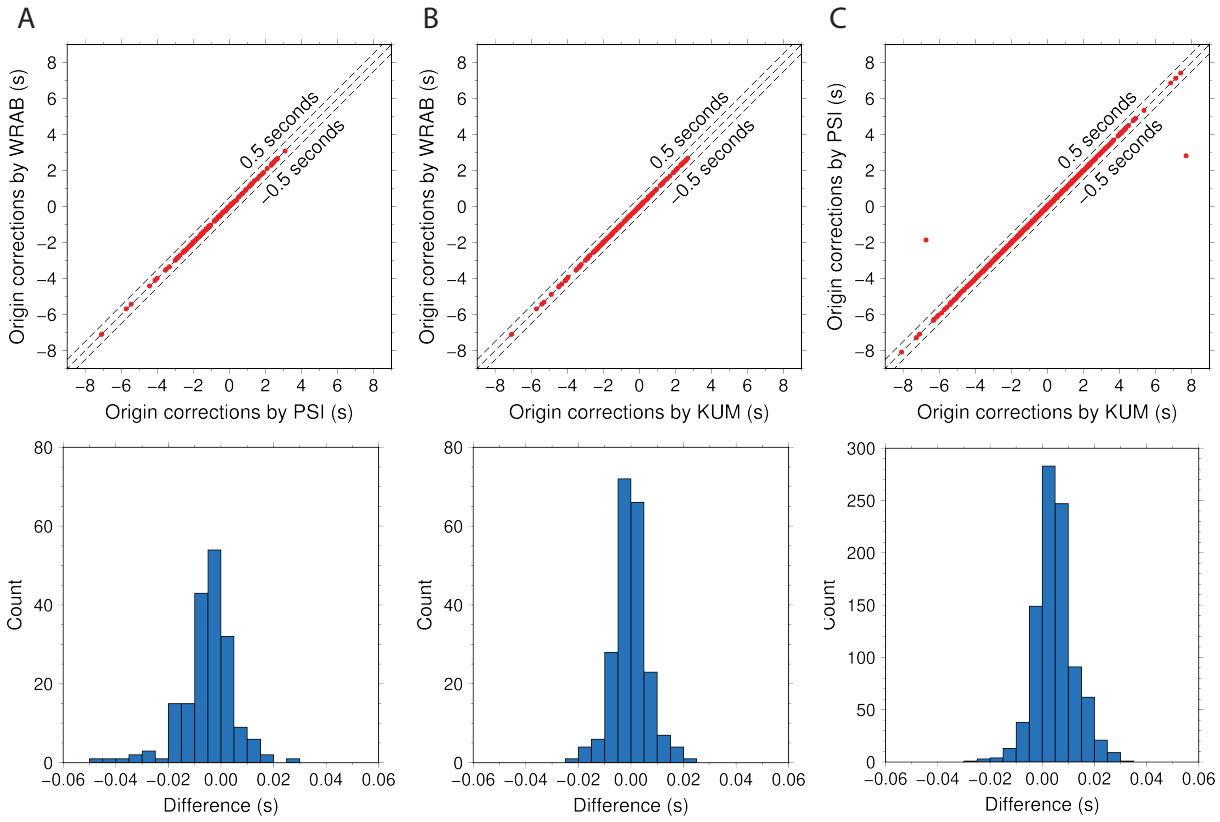

Figure S14: Comparing the earthquake origin time corrections using the three stations PSI, KUM, and WRAB. (Left) Comparison of origin time corrections derived from WRAB and PSI. The upper panel shows the two origin time corrections scattered against one another. The central dashed line shows the one-to-one line; the other two dashed lines correspond to ± 0.5 s discrepancy in the corrections, origin time discrepancy if one cycle is skipped in one of the records. The lower panel shows the histogram of the discrepancy between the origin time corrections. (Middle) The same as in the left panel but for WRAB and KUM. (Right) The same as in the left panels but for PSI and KUM. Note that there are two outliers that are outside of the plot range.

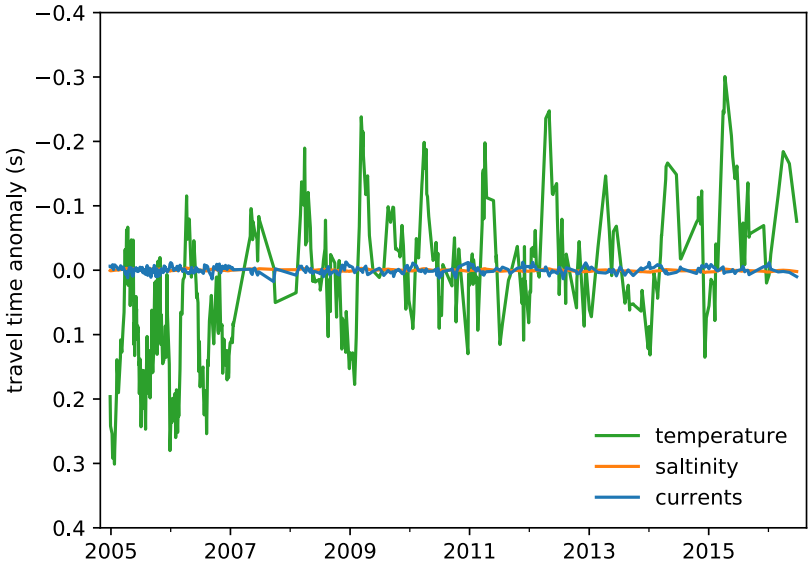

Figure S15: *T*-wave travel time anomalies due to temperature anomalies (green), salinity anomalies (orange), and non-tidal ocean current (blue). All effects are estimated from ECCO. The effect of salinity change is smaller than that of temperature change by more than an order of magnitude. The Doppler shift by ocean currents produces larger travel time anomalies than salinity variations, but they are still much smaller than the anomalies induced by temperature variations.

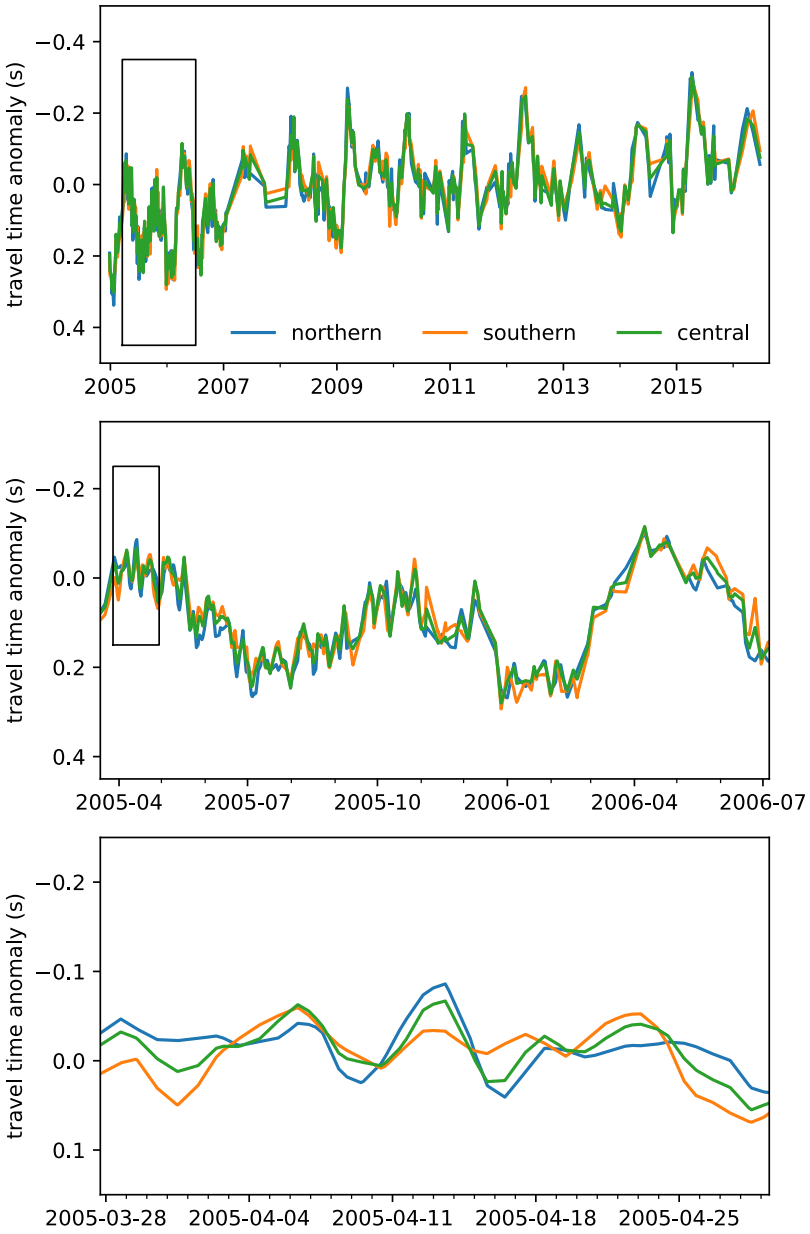

Figure S16: Quantification of lateral temperature variations using ECCO. Shown are the travel time anomalies inferred from ECCO along the three paths displayed in Fig. S3 and interpolated in time to the events used in this study. The middle and lower panels show successive zoom-ins on the early part of the time series (marked by black rectangles) when events were most abundant.

References and Notes

1. G. C. Johnson, J. M. Lyman, N. G. Loeb, Improving estimates of Earth's energy imbalance. *Nat. Clim. Chang.* **6**, 639–640 (2016). doi:10.1038/nclimate3043

2. C. Wunsch, Global Ocean Integrals and Means, with Trend Implications. *Annu. Rev. Mar. Sci.* **8**, 1–33 (2016). doi:10.1146/annurev-marine-122414-034040 Medline

3. J. Hansen, A. Lacis, D. Rind, G. Russell, P. Stone, I. Fung, R. Ruedy, J. Lerner, in *Climate Processes and Climate Sensitivity*, vol. 29, J. E. Hansen, T. Takahashi, Eds. (American Geophysical Union, 1984), pp. 130–163.

4. J. M. Gregory, Vertical heat transports in the ocean and their effect on time-dependent climate change. *Clim. Dyn.* **16**, 501–515 (2000). doi:10.1007/s003820000059

5. I. M. Held, M. Winton, K. Takahashi, T. Delworth, F. Zeng, G. K. Vallis, Probing the Fast and Slow Components of Global Warming by Returning Abruptly to Preindustrial Forcing. *J. Clim.* **23**, 2418–2427 (2010). doi:10.1175/2009JCLI3466.1

6. Y. Kostov, K. C. Armour, J. Marshall, Impact of the Atlantic meridional overturning circulation on ocean heat storage and transient climate change. *Geophys. Res. Lett.* **41**, 2108–2116 (2014). doi:10.1002/2013GL058998

7. K. von Schuckmann, M. D. Palmer, K. E. Trenberth, A. Cazenave, D. Chambers, N. Champollion, J. Hansen, S. A. Josey, N. Loeb, P.-P. Mathieu, B. Meyssignac, M. Wild, An imperative to monitor Earth's energy imbalance. *Nat. Clim. Chang.* **6**, 138–144 (2016). doi:10.1038/nclimate2876

8. C. Wunsch, Toward a Midlatitude Ocean Frequency–Wavenumber Spectral Density and Trend Determination. *J. Phys. Oceanogr.* **40**, 2264–2281 (2010). doi:10.1175/2010JPO4376.1

9. B. D. Dushaw, Ocean Acoustic Tomography in the North Atlantic. *J. Atmos. Ocean. Technol.* **36**, 183–202 (2019). doi:10.1175/JTECH-D-18-0082.1

10. S. C. Riser, H. J. Freeland, D. Roemmich, S. Wijffels, A. Troisi, M. Belbéoch, D. Gilbert, J. Xu, S. Pouliquen, A. Thresher, P.-Y. Le Traon, G. Maze, B. Klein, M. Ravichandran, F. Grant, P.-M. Poulain, T. Suga, B. Lim, A. Sterl, P. Sutton, K.-A. Mork, P. J. Vélez-Belchí, I. Ansorge, B. King, J. Turton, M. Baringer, S. R. Jayne, Fifteen years of ocean observations with the global Argo array. *Nat. Clim. Chang.* **6**, 145–153 (2016). doi:10.1038/nclimate2872

11. G. C. Johnson, S. G. Purkey, N. V. Zilberman, D. Roemmich, Deep Argo Quantifies Bottom Water Warming Rates in the Southwest Pacific Basin. *Geophys. Res. Lett.* **46**, 2662–2669 (2019). doi:10.1029/2018GL081685

12. E. A. Wilson, S. C. Riser, E. C. Campbell, A. P. S. Wong, Winter Upper-Ocean Stability and Ice–Ocean Feedbacks in the Sea Ice–Covered Southern Ocean. *J. Phys. Oceanogr.* **49**, 1099–1117 (2019). doi:10.1175/JPO-D-18-0184.1

13. D. Roemmich, J. Church, J. Gilson, D. Monselesan, P. Sutton, S. Wijffels, Unabated planetary warming and its ocean structure since 2006. *Nat. Clim. Chang.* **5**, 240–245 (2015). doi:10.1038/nclimate2513

14. J. P. Abraham, M. Baringer, N. L. Bindoff, T. Boyer, L. J. Cheng, J. A. Church, J. L. Conroy, C. M. Domingues, J. T. Fasullo, J. Gilson, G. Goni, S. A. Good, J. M. Gorman, V. Gouretski, M. Ishii, G. C. Johnson, S. Kizu, J. M. Lyman, A. M. Macdonald, W. J. Minkowycz, S. E. Moffitt, M. D. Palmer, A. R. Piola, F. Reseghetti, K. Schuckmann, K. E. Trenberth, I. Velicogna, J. K. Willis, A review of global ocean temperature observations: Implications for ocean heat content estimates and climate change. *Rev. Geophys.* **51**, 450–483 (2013). doi:10.1002/rog.20022

15. W. Munk, C. Wunsch, Ocean acoustic tomography: A scheme for large scale monitoring. *Deep-Sea Res.* **26**, 123–161 (1979). doi:10.1016/0198-0149(79)90073-6

16. W. H. Munk, A. M. G. Forbes, Global Ocean Warming: An Acoustic Measure? *J. Phys. Oceanogr.* **19**, 1765–1778 (1989). doi:10.1175/1520-0485(1989)019<1765:GOWAAM>2.0.CO;2

17. The ATOC Consortium, Ocean Climate Change: Comparison of Acoustic Tomography, Satellite Altimetry, and Modeling. *Science* **281**, 1327–1332 (1998). doi:10.1126/science.281.5381.1327 Medline

18. P. F. Worcester, B. D. Cornuelle, M. A. Dzieciuch, W. H. Munk, B. M. Howe, J. A. Mercer, R. C. Spindel, J. A. Colosi, K. Metzger, T. G. Birdsall, A. B. Baggeroer, A test of basin-scale acoustic thermometry using a large-aperture vertical array at 3250-km range in the eastern North Pacific Ocean. *J. Acoust. Soc. Am.* **105**, 3185–3201 (1999). doi:10.1121/1.424649

19. B. D. Dushaw, P. F. Worcester, W. H. Munk, R. C. Spindel, J. A. Mercer, B. M. Howe, K. Metzger Jr., T. G. Birdsall, R. K. Andrew, M. A. Dzieciuch, B. D. Cornuelle, D. Menemenlis, A decade of acoustic thermometry in the North Pacific Ocean. *J. Geophys. Res.* **114**, C07021 (2009). doi:10.1029/2008JC005124

20. N. Oreskes, in *Science and Technology in the Global Cold War*, N. Oreskes, J. Krige, Eds. (MIT Press, 2014), pp. 141–188.

21. C. G. Fox, H. Matsumoto, T.-K. A. Lau, Monitoring Pacific Ocean seismicity from an autonomous hydrophone array. *J. Geophys. Res. Solid Earth* **106**, 4183–4206 (2001). doi:10.1029/2000JB900404

22. R. P. Dziak, P- and T-Wave Detection Thresholds, Pn Velocity Estimate, and Detection of Lower Mantle and Core P-Waves on Ocean Sound-Channel Hydrophones at the Mid-Atlantic Ridge. *Bull. Seismol. Soc. Am.* **94**, 665–677 (2004). doi:10.1785/0120030156

23. E. A. Okal, in *Advances in Geophysics*, vol. 49, R. Dmowska, Ed. (Elsevier, 2008), pp. 1–65.

24. J. S. Buehler, P. M. Shearer, *T* phase observations in global seismogram stacks. *Geophys. Res. Lett.* **42**, 6607–6613 (2015). doi:10.1002/2015GL064721

25. D. Linehan, Earthquakes in the West Indian region. *EOS Trans. Am. Geophys. Union* **21**, 229–232 (1940).

26. I. Tolstoy, M. Ewing, The T Phase of Shallow-Focus Earthquakes. *Bull. Seismol. Soc. Am.* **40**, 25–51 (1950).

27. J. Talandier, E. A. Okal, On the mechanism of conversion of seismic waves to and from T waves in the vicinity of island shores. *Bull. Seismol. Soc. Am.* **88**, 621–632 (1998).

28. W. Munk, P. Worcester, C. Wunsch, *Ocean Acoustic Tomography* (Cambridge Univ. Press, 1995).

29. D. Komatitsch, J. Tromp, Introduction to the spectral element method for three-dimensional seismic wave propagation. *Geophys. J. Int.* **139**, 806–822 (1999). doi:10.1046/j.1365-246x.1999.00967.x

30. E. A. Okal, J. Talandier, *T* waves from the great 1994 Bolivian deep earthquake in relation to channeling of *S* wave energy up the slab. *J. Geophys. Res.* **102**, 27421–27437 (1997). doi:10.1029/97JB02718

31. M. Sáez, S. Ruiz, Controls on the *T* Phase Energy Fluxes Recorded on Juan Fernandez Island by Continental Seismic Wave Paths and Nazca Bathymetry. *Geophys. Res. Lett.* **45**, 2610–2617 (2018). doi:10.1002/2017GL076790

32. N. Uchida, R. Bürgmann, Repeating Earthquakes. *Annu. Rev. Earth Planet. Sci.* **47**, 305–332 (2019). doi:10.1146/annurev-earth-053018-060119

33. W. Yu, T.-R. A. Song, P. G. Silver, Temporal Velocity Changes in the Crust Associated with the Great Sumatra Earthquakes. *Bull. Seismol. Soc. Am.* **103**, 2797–2809 (2013). doi:10.1785/0120120354

34. X. Song, P. G. Richards, Seismological evidence for differential rotation of the Earth's inner core. *Nature* **382**, 221–224 (1996). doi:10.1038/382221a0

35. G. Forget, J. Campin, P. Heimbach, C. N. Hill, R. M. Ponte, C. Wunsch, ECCO version 4: An integrated framework for non-linear inverse modeling and global ocean state estimation. *Geosci. Model Dev.* **8**, 3071–3104 (2015). doi:10.5194/gmd-8-3071-2015

36. ECCO Consortium, I. Fukumori, O. Wang, I. Fenty, G. Forget, P. Heimbach, R. M. Ponte, ECCO Central Estimate (Version 4, Release 4) (2020); https://ecco.jpl.nasa.gov/drive/files/Version4/Release4.

37. D. Roemmich, J. Gilson, The 2004–2008 mean and annual cycle of temperature, salinity, and steric height in the global ocean from the Argo Program. *Prog. Oceanogr.* **82**, 81–100 (2009). doi:10.1016/j.pocean.2009.03.004

38. B. M. Howe, J. Miksis-Olds, E. Rehm, H. Sagen, P. F. Worcester, G. Haralabus, Observing the Oceans Acoustically. *Front. Mar. Sci.* **6**, 426 (2019). doi:10.3389/fmars.2019.00426

39. A. Sukhovich, S. Bonnieux, Y. Hello, J. O. Irisson, F. J. Simons, G. Nolet, Seismic monitoring in the oceans by autonomous floats. *Nat. Commun.* **6**, 8027 (2015). doi:10.1038/ncomms9027 Medline

40. B. Gutenberg, C. F. Richter, Frequency of earthquakes in California. *Bull. Seismol. Soc. Am.* **34**, 185–188 (1944).

41. Argo, Argo float data and metadata from Global Data Assembly Centre (Argo GDAC), SEANOE (2020); https://doi.org/10.17882/42182.

42. T. J. McDougall, P. M. Barker, "Getting started with TEOS-10 and the Gibbs Seawater (GSW) Oceanographic Toolbox" (SCOR/IAPSO WG127, 2011); www.teos-10.org/pubs/Getting_Started.pdf.

43. E. K. Skarsoulis, B. D. Cornuelle, Travel-time sensitivity kernels in ocean acoustic tomography. *J. Acoust. Soc. Am.* **116**, 227–238 (2004). doi:10.1121/1.1753292

44. B. D. Dushaw, Assessing the horizontal refraction of ocean acoustic tomography signals using high-resolution ocean state estimates. *J. Acoust. Soc. Am.* **136**, 122–129 (2014). doi:10.1121/1.4881928 Medline

45. J. Tromp, D. Komatitsch, Q. Liu, Spectral-Element and Adjoint Methods in Seismology. *Commun. Comput. Phys.* **3**, 1–32 (2008).

46. M. Kobayashi, S. Takemura, K. Yoshimoto, Frequency and distance changes in the apparent *P* -wave radiation pattern: Effects of seismic wave scattering in the crust inferred from dense seismic observations and numerical simulations. *Geophys. J. Int.* **202**, 1895–1907 (2015). doi:10.1093/gji/ggv263

47. C. D. de Groot-Hedlin, J. A. Orcutt, Excitation of *T*-phases by seafloor scattering. *J. Acoust. Soc. Am.* **109**, 1944–1954 (2001). doi:10.1121/1.1361057 Medline

48. M. Park, R. I. Odom, D. J. Soukup, Modal scattering: A key to understanding oceanic T-waves. *Geophys. Res. Lett.* **28**, 3401–3404 (2001). doi:10.1029/2001GL013472

49. H. Sato, M. C. Fehler, T. Maeda, *Seismic Wave Propagation and Scattering in the Heterogeneous Earth: Second Edition* (Springer, 2012).

50. Y. Luo, J. Tromp, B. Denel, H. Calandra, 3D coupled acoustic-elastic migration with topography and bathymetry based on spectral-element and adjoint methods. *Geophysics* **78**, S193–S202 (2013). doi:10.1190/geo2012-0462.1

51. Q. Liu, J. Tromp, Finite-Frequency Kernels Based on Adjoint Methods. *Bull. Seismol. Soc. Am.* **96**, 2383–2397 (2006). doi:10.1785/0120060041

52. F. M. Graeber, P. F. Piserchia, Zones of *T* -wave excitation in the NE Indian ocean mapped using variations in backazimuth over time obtained from multi-channel correlation of IMS hydrophone triplet data. *Geophys. J. Int.* **158**, 239–256 (2004). doi:10.1111/j.1365-246X.2004.02301.x

53. A. M. Dziewonski, D. L. Anderson, Preliminary reference Earth model. *Phys. Earth Planet. Inter.* **25**, 297–356 (1981). doi:10.1016/0031-9201(81)90046-7

54. N. Deichmann, M. Garcia-Fernandez, Rupture geometry from high-precision relative hypocentre locations of microearthquake clusters. *Geophys. J. Int.* **110**, 501–517 (1992). doi:10.1111/j.1365-246X.1992.tb02088.x

55. J. Yao, D. Tian, L. Sun, L. Wen, Temporal Change of Seismic Earth's Inner Core Phases: Inner Core Differential Rotation or Temporal Change of Inner Core Surface? *J. Geophys. Res. Solid Earth* **124**, 6720–6736 (2019). doi:10.1029/2019JB017532

56. G. D. Egbert, S. Y. Erofeeva, Efficient Inverse Modeling of Barotropic Ocean Tides. *J. Atmos. Ocean. Technol.* **19**, 183–204 (2002). doi:10.1175/1520-0426(2002)019<0183:EIMOBO>2.0.CO;2